Spatial atomic layer deposition for coating flexible porous Li-ion battery electrodes

Alexander S. Yersak, Kashish Sharma, Jasmine M. Wallas, and Arrelaine A. Dameron
Department of Chemistry and Biochemistry, University of Colorado, Boulder, Colorado 80309

Xuemin Li and Yongan Yang
Department of Chemistry, Colorado School of Mines, Golden, Colorado 80401

Katherine E. Hurst, Chunmei Ban, and Robert C. Tenent
National Renewable Energy Laboratory, Golden, Colorado 80401

Steven M. George[a)]
Department of Chemistry and Biochemistry, University of Colorado, Boulder, Colorado 80309 and
Department of Mechanical Engineering, University of Colorado, Boulder, Colorado 80309

Ultrathin atomic layer deposition (ALD) coatings on the electrodes of Li-ion batteries can enhance the capacity stability of the Li-ion batteries. To commercialize ALD for Li-ion battery production, spatial ALD is needed to decrease coating times and provide a coating process compatible with continuous roll-to-roll (R2R) processing. The porous electrodes of Li-ion batteries provide a special challenge because higher reactant exposures are needed for spatial ALD in porous substrates. This work utilized a modular rotating cylinder spatial ALD reactor operating at rotation speeds up to 200 revolutions/min (RPM) and substrate speeds up to 200 m/min. The conditions for spatial ALD were adjusted to coat flexible porous substrates. The reactor was initially used to characterize spatial Al_2O_3 and ZnO ALD on flat, flexible metalized polyethylene terephthalate foils. These studies showed that slower rotation speeds and spacers between the precursor module and the two adjacent pumping modules could significantly increase the reactant exposure. The modular rotating cylinder reactor was then used to coat flexible, model porous anodic aluminum oxide (AAO) membranes. The uniformity of the ZnO ALD coatings on the porous AAO membranes was dependent on the aspect ratio of the pores and the reactant exposures. Larger reactant exposures led to better uniformity in the pores with higher aspect ratios. The reactant exposures were increased by adding spacers between the precursor module and the two adjacent pumping modules. The modular rotating cylinder reactor was also employed for Al_2O_3 ALD on porous $LiCoO_2$ (LCO) battery electrodes. Uniform Al coverages were obtained using spacers between the precursor module and the two adjacent pumping modules at rotation speeds of 25 and 50 RPM. The LCO electrodes had a thickness of $\sim$49 μm and pores with aspect ratios of $\sim$12–25. Coin cells were then constructed using the ALD-coated LCO electrodes and were tested to determine their battery performance. The capacity of the Al_2O_3 ALD-coated LCO battery electrodes was measured versus the number of charge-discharge cycles. Both temporal and spatial ALD processing methods led to higher capacity stability compared with uncoated LCO battery electrodes. The results for improved battery performance were comparable for temporal and spatial ALD-coated electrodes. The next steps are also presented for scale-up to R2R spatial ALD using the modular rotating cylinder reactor. *Published by the AVS.* https://doi.org/10.1116/1.5006670

I. INTRODUCTION

Atomic layer deposition (ALD) is based on sequential, self-limiting surface reactions.[1] The self-limiting nature of ALD yields conformal films with subnanometer control over coating thickness.[1] A key advantage of ALD over other coating processes, such as chemical vapor deposition, physical vapor deposition, and sol-gel deposition, is the ability of ALD to infiltrate and uniformly coat high aspect ratio features.[1,2] ALD can conformally coat high surface area structures with aspect ratios as large as 1000.[2]

The ability to coat high aspect ratio structures is important for ALD on porous Li-ion battery electrodes. Initial studies of Al_2O_3 ALD on porous $LiCoO_2$ (LCO) cathode electrodes and porous graphite anode electrodes revealed large enhancement of capacity stability after the application of ALD coatings.[3,4] Additional investigations have obtained similar results[5–8] and also demonstrated the value of ALD coatings on other Li-ion battery materials.[9–12] In addition, Al_2O_3 ALD films are useful to coat separators for Li-ion batteries.[13] These promising results have motivated the incorporation of ALD coatings in Li-ion battery production.

ALD can be performed using either temporal or spatial ALD.[14] During temporal ALD, the substrate is held in a fixed position and the reactants are separated in time.[14] During spatial ALD, the substrate moves through separated gas zones of constantly flowing reactants.[14] Spatial ALD can generally be much faster (up to >10×) than temporal ALD

[a)]Electronic mail: Steven.George@Colorado.Edu

because the growth rates in spatial ALD are determined primarily by substrate translation speeds rather than the purge times during temporal ALD.

Spatial ALD can be performed using a number of different designs based primarily on the gap between the gas source head and the substrate.[14] These designs include a translating gas source head or substrate moving horizontally back-and-forth with a gap of $\sim$30–100 μm defined either by mechanical separation or a gas bearing;[15–17] a substrate spinning underneath a gas source head with the gap of $\sim$20 μm defined by a gas bearing;[18] and a rotating cylinder design with the gap of $\sim$1 mm defined by two concentric cylinders.[19–22] Another design is based on a "serpentine" web moving through spatially separated reactants[23] or a "closed loop" flexible web moving under a gas source head.[24] The serpentine spatial ALD reactor is a true roll-to-roll (R2R) ALD reactor.[23] A rotating cylinder spatial ALD reactor can also be adapted for roll-to-roll processing of flexible foil.[25]

Special challenges are encountered for spatial ALD on porous or high aspect ratio substrates.[21,26,27] With rapid substrate speeds through the reactant zones, shorter reactant exposure times can limit the number of reactant collisions with the substrate and decrease the ALD growth rate. Previous spatial ALD investigations have shown that faster substrate speeds can restrict growth rates even for flat substrates.[22,25,28,29] For spatial ALD on porous substrates, mass transport limitations become even more important.[21,26] Studies on model porous anodic aluminum oxide (AAO) membranes revealed that spatial ALD coatings could be uniform or nonuniform depending on the aspect ratio and the exposure times in the reactant zone.[21]

Our earlier studies have investigated Al_2O_3 spatial ALD on flat, flexible substrates using a rotating cylinder reactor.[22] Additional studies have explored the ability of spatial ALD to infiltrate porous materials using flexible, porous AAO membranes.[21] Spatial ALD and temporal ALD studies have shown that infiltration into porous materials is a function of the reactant exposure.[2,21,30] When the reactions are not reactant supply-limited, the reactant exposure during spatial ALD is defined by the substrate speed, width of the reactant zone, and reactant pressure. In comparison, the reactant exposure during temporal ALD is defined by the exposure time and the reactant pressure.

In this study, the reaction conditions during spatial ALD were tuned to coat porous flexible substrates. Initially, the growth rates for Al_2O_3 ALD and ZnO ALD on flat, flexible metalized polyethylene terephthalate (PET) substrates were examined using the spatial ALD rotating cylinder reactor at 40 °C. These studies explored the effect of spacers between the precursor module and the pumping modules on the reactant exposures. The rotating cylinder reactor was configured with 0, 2, 4, and 6 total spacers between the precursor module and the two adjacent pumping modules. Additional studies were conducted for ZnO ALD on porous flexible AAO membranes using different numbers of total spacers that lengthen the reactant exposure time. These studies determined if longer reactant exposure times defined by the

spacers could increase infiltration into the porous AAO membrane.

Al_2O_3 spatial ALD coatings were then deposited on LCO electrodes at 60 °C. In these studies, the reactant exposure was varied by the rotating cylinder speed. The Al_2O_3 ALD coatings were deposited at 10, 25, and 50 revolutions/min (RPM) using trimethylaluminum (TMA) and ozone as the reactants using four total spacers between the TMA precursor module and the two adjacent pumping modules.[31] Cross-sectional energy dispersive x-ray spectroscopy (EDS) was used to measure the depth of Al_2O_3 ALD infiltration into the LCO electrodes versus rotating cylinder speed. These samples were taken from positions on the centerline of the rotating cylinder.

Coin cells were also assembled and tested with and without temporal Al_2O_3 ALD coatings or spatial Al_2O_3 ALD coatings on the LCO electrodes. Results were obtained using three different temporal ALD reactors that operated under either static or continuous flow conditions. Coin cell results were also obtained for ALD-coated electrodes prepared with the spatial ALD rotating cylinder reactor operating at 10, 25, and 50 RPM. These results demonstrate the potential of temporal and spatial ALD as an electrode coating technology to enhance the capacity stability of Li-ion batteries. The promising coin cell results obtained using spatial ALD provide motivation for the commercialization of spatial ALD using roll-to-roll processing.

II. EXPERIMENT

A. Spatial ALD reactor and modules

Figure 1 shows cross-sections of the modular rotating cylinder reactor for spatial ALD. This rotating cylinder reactor has been described in detail in earlier publications.[21,22] The inner rotating cylinder has a diameter of $\sim$32 cm and a circumference of 1 m. The inner rotating cylinder moves under the modules on the outer cylinder. These modules have a width of 25 mm and a length of $\sim$190 mm and attach on the outside of the outer cylinder. A slit under each module separates the module and the inside of the outer cylinder. The slits define the precursor, pumping, purging, and spacer zones. The modular design of the rotating cylinder reactor enables the placement of 31 dosing, pumping, purging, or spacer zones on the outside of the outer cylinder.

The modules can be easily moved to optimize the reactor configuration. The 31 modules on the outside of the outer cylinder subtend a solid angle of 270° relative to the cylinder axis. There is also a blank space that subtends a solid angle of 90° relative to the cylinder axis at the bottom of the outer cylinder. This blank space is for future development to achieve true roll-to-roll operation. This blank space will be used to bring the web in and out of the rotating cylinder reactor.

The distance between the fixed outer cylinder and the rotating inner cylinder is $\sim$750 μm. This distance defines a conductance gap between the outer and inner cylinders. The slits under each module are open to the conductance gap. These slits have a length of 165 mm and a width of $\sim$8 mm.
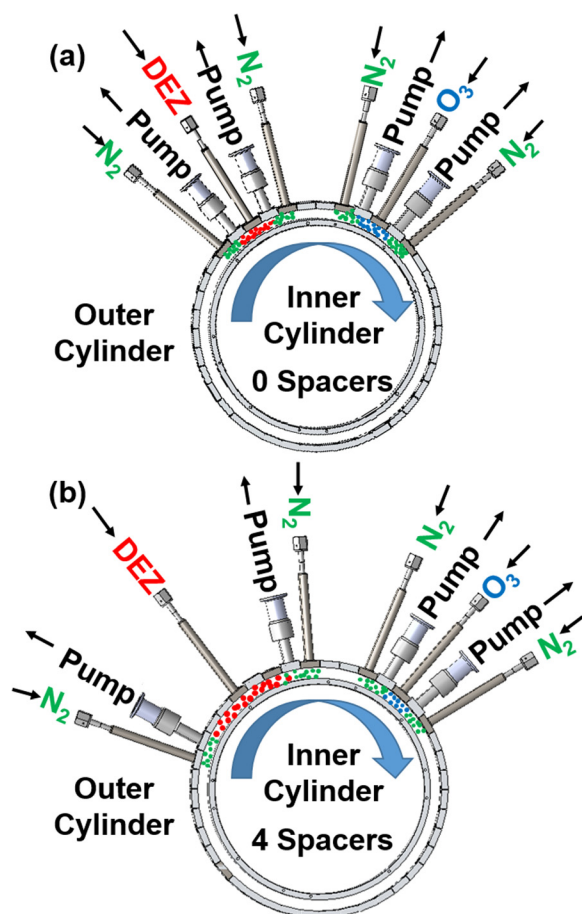
FIG. 1. (Color online) Cross-section of the rotating cylinder reactor configured for ZnO spatial ALD with (a) no spacers and (b) four total spacers between the DEZ precursor module and the two adjacent pumping modules.

The dosing modules were designed using computational fluid dynamics to ensure that the reactant gases completely filled the entire length of the slits.[22] The modular design allows for the adjustment of the reactant exposure time by adding spacers between the modular precursor inlet and pumping outlet modules. The reactant exposure time is estimated from the rotation speed of the inner cylinder and the distance between the center of the precursor module and center of the pumping module. The pitch between adjacent modules is 25 mm.

In the cross-sections of the rotating cylinder reactor displayed in Fig. 1, there are two reactant exposures per rotation for one complete ALD cycle per rotation. In Fig. 1(a), there are no spacers between the precursor and pumping modules. At a given rotation speed, this configuration yields the shortest reactant exposure. In Fig. 1(b), there are two spacers between the precursor and each pumping module or four total spacers between the precursor and the two adjacent pumping modules. The spacers will yield a longer reactant exposure compared with the configuration with no spacers.

The reactant exposure time for a rotation speed of 210 RPM and six total spacers (three spacers on either side of the reactant) is calculated to be ~28.5 ms. The rotation speed of 210 RPM is equivalent to a substrate speed of 210 m/min. The distance between the center of the precursor module and

the center of the pumping module across three spacers is 100 mm. The reactant exposure time is based on only one side of the reactant zone because the movement of the rotating cylinder acts like a pump and transports the reactant in the direction of the moving rotating cylinder. The reactant exposure is estimated from the reactant exposure time and the reactant pressure in the gap region of the rotating cylinder reactor.

B. Al_2O_3 and ZnO ALD on metalized PET substrates

Al_2O_3 and ZnO ALD coatings were grown on flat, flexible titanium metallized PET polymer substrates with a thickness of ~130 μm. The temperature of the rotating cylinder reactor was 40 °C. Al_2O_3 coatings were grown using TMA (AKZO Nobel HPMO) and ozone.[31] The TMA mass flow rate was ~34 mg/min. ZnO coatings were grown using diethylzinc (DEZ) (AKZO Nobel HPMO) and ozone. Ozone was generated using an O3ONIA ozone generator with oxygen [Airgas, ultrahigh purity (99.993%)]. The product O_3 had a concentration of ~10% in the O_2 gas. The spatial ALD reactor was configured with 0, 2, 4, or 6 total spacers between the precursor module and the two adjacent pumping modules. The rotation speed of the inner rotating cylinder was varied between 53, 100, and 210 RPM.

The process pressures measured in the dosing modules for TMA, DEZ, and ozone were ~12, ~10 and ~14 Torr, respectively. Each reactant was pumped with a separate dual stage rotary vane mechanical pump. The central chamber of the rotating cylinder reactor was pumped with one dual stage rotary vane mechanical pump to a base pressure of ~40 mTorr with no N_2 flowing in the purge modules. Purging was achieved using a N_2 flow of 300 sccm in each purging module.

The thicknesses of the Al_2O_3 and ZnO coatings were determined using spectroscopic ellipsometry (J. A. Woolman Co., Inc., M2000U). A standard Cauchy model was used to fit the refractive index using the An, Bn, and Cn Cauchy fit parameters. A native oxide was present on the surface of the titanium-metalized PET foil.

C. ZnO ALD on AAO membranes

ZnO ALD was performed on flexible, porous AAO membranes with pore diameters varying from 10 to 100 nm. The pores in the AAO membrane had a length of 25 μm and were closed at the end. The rotating cylinder reactor was configured with 0, 2, and 4 total spacers between the DEZ module and the two adjacent pumping modules. The rotation speed of the rotating inner cylinder varied from 10 to 100 RPM. The number of cycles required to obtain the desired ZnO thicknesses was determined from previous studies of ZnO ALD on flat, flexible substrates using the rotating cylinder reactor.[22] One change from the reaction conditions reported in Sec. II B was that the central chamber of the rotating cylinder reactor was pumped with two dual stage rotary vane mechanical pumps to reduce the pump down time.

A scanning electron microscope (SEM) (JEOL JSM-7401F) with an EDS unit was used to measure Zn in the

AAO pores. These SEM measurements have been described in an earlier publication.[21] Cross-sectional line scans with a spatial resolution of $\sim 1\,\mu m$ were recorded with an accelerating voltage of 10 keV.

D. Al$_2$O$_3$ ALD on LCO Li-ion battery electrodes

Al$_2$O$_3$ ALD coatings were deposited on LCO electrodes using the rotating cylinder reactor. The LCO electrodes were obtained from the Argonne National Lab. The porous LCO electrodes were $\sim 49\,\mu m$ thick and had a porosity of 35%. The Al$_2$O$_3$ ALD was performed with rotation speeds for the inner rotating cylinder of 10, 25, and 50 RPM. The rotating cylinder reactor was configured with four total spacers between the TMA and ozone precursor modules and the two adjacent pumping modules. The reactor temperature was 60 °C.

The gas conductance in the LCO electrode is defined by the gaps between the LCO particles. For particles of 5 and 10 μm in diameter, the gaps between particles appear to be ~ 2 and $\sim 4\,\mu m$, respectively. These gaps can be visualized using SEM as shown in Sec. III C. The aspect ratio for the pores in the LCO electrodes can be estimated using the gap size and the electrode thickness. For gaps of ~ 2 and $\sim 4\,\mu m$, the aspect ratios are ~ 25 and ~ 12, respectively. This estimate does not account for tortuosity.

Purging was defined using a N$_2$ flow of 250 sccm in each purging module. The process pressures measured in the dosing modules for TMA and ozone were 3–4 and 4–5 Torr, respectively. A large fraction of this pressure is attributed to the N$_2$ pressure. For the cross-sectional EDS measurements, the Al$_2$O$_3$ ALD-coated LCO electrodes were prepared using 2000 Al$_2$O$_3$ ALD cycles. This number of Al$_2$O$_3$ ALD cycles is much larger than the four Al$_2$O$_3$ ALD cycles utilized for battery testing using coin cells. These thick Al$_2$O$_3$ coatings were needed to obtain measurable Al EDS signals that were greater than the Al EDS measurement noise of ~ 1 wt. %. A scanning electron microscope (JEOL JSM 6480LV) with an EDS unit was used to measure the Al signals in the porous LCO electrodes. The accelerating voltage was set to 15 keV.

Temporal Al$_2$O$_3$ ALD coatings were also deposited on porous LCO electrodes using three temporal ALD reactors. Two of these temporal ALD reactors were the Beneq TFS 200 and a home-built reactor that were located at the National Renewable Energy Laboratory. The third temporal ALD reactor was a home-built reactor at the University of Colorado. Information on the reactants, substrate temperature, and dosing scheme used in these three reactors is given in Table I.

E. Coin cell assembly and testing

Coin cells were assembled using bare or Al$_2$O$_3$ ALD-coated LCO electrodes and graphite anodes in an Ar-filled glovebox at room temperature. The active material loading was ~ 10 mg/cm^2 on the cathodes and ~ 5 mg/cm^2 on the anodes. The electrolytes were composed of 1.2 M LiPF$_6$ dissolved in a mixture of ethylene carbonate and ethyl-methyl carbonate (3:7 by weight). The separators were Celgard 2325 [a porous polypropylene (PP)/polyethylene/PP trilayer film]. Galvanostatic charge–discharge cycling was performed at room temperature with the voltage window of 3.3–4.5 V. The current used for coin cell cycling was 1 C rate based on the mass of LCO (1 C rate = 140 mA h/g).

III. RESULTS AND DISCUSSION

A. Al$_2$O$_3$ and ZnO ALD on metalized PET

Figure 2(a) shows the Al$_2$O$_3$ ALD growth rate at 40 °C using TMA and O$_3$ as the reactants versus rotating speeds of 53, 100, and 210 RPM. The reactor was configured with 0, 2, 4, and 6 total spacers between the TMA precursor module and the two adjacent pumping modules. For these experiments, the total pressure in the TMA module was 9 Torr and the pressure in the center of the rotating cylinder reactor was 7 Torr. Most of these pressures are attributed to the N$_2$ partial pressure. The Al$_2$O$_3$ growth rate increases at lower rotation rates and for more spacers between the TMA precursor module and the two adjacent pumping modules.

The Al$_2$O$_3$ ALD growth rate is the highest for the six total spacers at the lowest rotation speed of 53 RPM. These conditions yield the largest reactant exposure during spatial ALD. The six total spacers extend the TMA pressure over a greater length in the conductance gap. This larger TMA reactant zone yields a larger TMA exposure. The smaller number of spacers led to shorter exposure times and lower growth rates at various rotation speeds.

Figure 2(b) displays the TMA exposure time versus rotation speeds of 53, 100, and 210 RPM for the reactor configured with 0, 2, 4, and 6 total spacers between the TMA precursor module and the two adjacent pumping modules. The rotation speed of 53 RPM produces the longest reactant exposure time and the largest Al$_2$O$_3$ growth rate. A decrease in the Al$_2$O$_3$ ALD growth rate is observed with fewer spacers and shorter TMA exposure times. A similar decrease in the Al$_2$O$_3$ ALD growth rate versus substrate speed has been observed previously for this rotating cylinder reactor and for other spatial ALD reactors.[21,22,24,32–34]

The Al$_2$O$_3$ growth rate in Fig. 2(a) begins to display self-limiting behavior at 53 RPM for 2, 4, and 6 spacers. The

TABLE I. Process parameters for temporal ALD coatings on porous LCO electrodes. Timing sequence: d, p, e, and h represent the reactant dose, N$_2$/Ar purge, evacuation, and hold, respectively. Times are given in seconds.

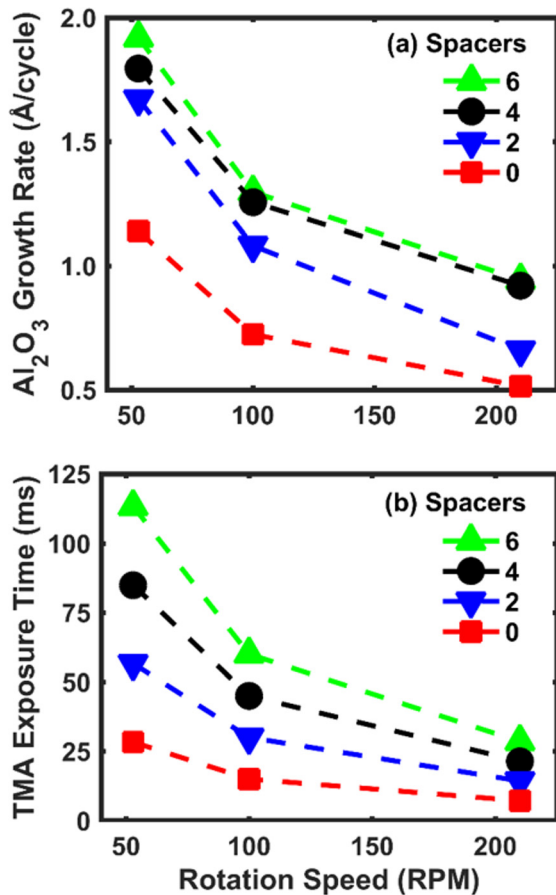| Reactor	Tool/flow type	Chemistry	Substrate temp. (°C)	Metalorganic sequence	Oxidant sequence
I	Beneq TFS 200/continuous	TMA/water	120	d/p/d/p (0.3/5/0.3/8)	d/p/d/p (0.3/5/0.3/8)
II	Home-built/static	TMA/water	120	d/h/p/e (1/60/30/30)	d/h/p/e (3/60/60/30)
III	Home-built/static	TMA/ozone	60	d/h/p/e (1/300/240/30)	d/h/p/e (0.5/300/240/30)

FIG. 2. (Color online) (a) Al_2O_3 ALD growth rate at $40\,°C$ and (b) TMA exposure time vs rotation speed with 0, 2, 4, and 6 total spacers between the TMA precursor module and the two adjacent pumping modules.

FIG. 3. (Color online) (a) ZnO ALD growth rate at $40\,°C$ and (b) DEZ exposure time vs rotation speed with 0, 2, 4, and 6 total spacers between the DEZ precursor module and the two adjacent pumping modules.

limiting Al_2O_3 growth rate appears to be close to the maximum Al_2O_3 ALD growth rate of $\sim1.9\,Å/cycle$ observed at 53 RPM and six total spacers. This Al_2O_3 ALD growth rate is higher than the typical Al_2O_3 ALD growth rate of $1.1–1.2\,Å/cycle$ for Al_2O_3 ALD using TMA and H_2O as the reactants from 33 to $177\,°C$.[35] The higher Al_2O_3 growth rates of $\sim1.9\,Å/cycle$ may partly result from different surface chemistry using TMA and ozone at $40\,°C$. Plasma Al_2O_3 ALD with TMA and O_2 plasma as the reactants has also observed higher growth rates of $\sim1.7\,Å/cycle$ at $25\,°C$.[36]

The higher Al_2O_3 growth rates of $\sim1.9\,Å/cycle$ using TMA and ozone as the reactants may result from higher formate and carbonate coverages at low temperatures.[31] Earlier Fourier transform infrared studies have revealed that formate and carbonate groups decompose and leave hydroxyl groups at $200\,°C$ during Al_2O_3 ALD using TMA and ozone.[31] The coverage of these formate and carbonate surface species may increase at lower temperatures and lead to higher apparent Al_2O_3 ALD growth rates. Al_2O_3 ALD growth experiments were also performed using TMA and ozone at $60\,°C$. The Al_2O_3 growth rate decreased from $\sim1.9\,Å/cycle$ at $40\,°C$ to $\sim1.2\,Å/cycle$ at $60\,°C$.

Figure 3(a) shows the ZnO growth rate, and Fig. 3(b) displays the DEZ exposure time for rotation rates of 53, 100, and 210 RPM with the reactor configured with 0, 2, 4, and 6
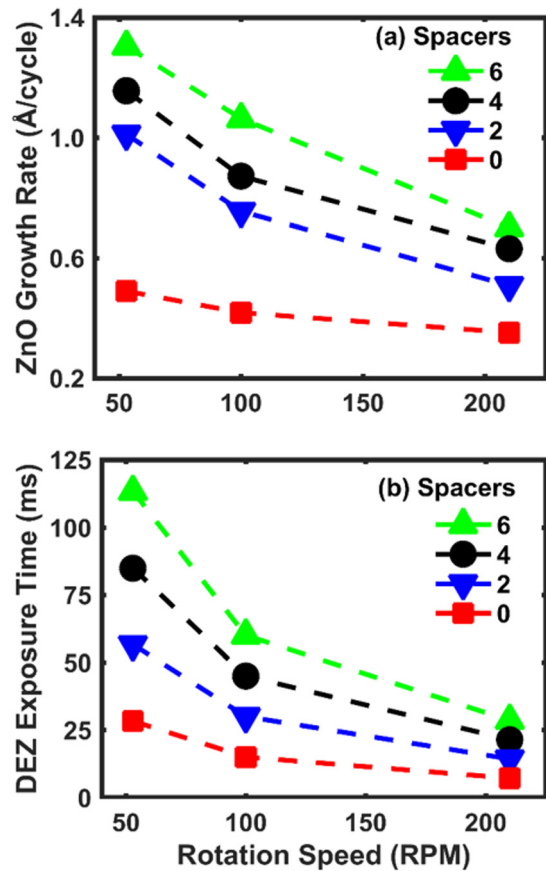
total spacers between the DEZ precursor and the two adjacent pumping modules. The results in Fig. 3 for ZnO ALD are similar to the results in Fig. 2 for Al_2O_3 ALD. For these experiments, the temperature was $40\,°C$. The total pressure in the DEZ module was 8 Torr, and the pressure in the center of the rotating cylinder reactor was 7 Torr. Most of these pressures are again assigned to the N_2 partial pressures.

The ZnO growth rate increases at higher reactant exposure time. The higher reactant exposure times are obtained at lower rotation rates and for more total spacers between the TMA precursor module and the two adjacent pumping modules. The maximum ZnO ALD growth rate was $1.3\,Å/cycle$ at 50 RPM and six total spacers. The ZnO ALD growth rate has not reached the self-limiting growth rate because the ZnO ALD growth rate is still increasing steadily with the number of spacers at 50 RPM. In addition, the ZnO growth rates scale well with the DEZ exposure times in Fig. 3(b). These observations are consistent with the ZnO ALD not obtaining the self-limiting growth rate under these reaction conditions.

B. ZnO ALD on porous AAO membranes

The uniformity of the ZnO coverage in porous AAO membranes depends on the reactant exposures and the aspect ratio of the AAO membrane. For a fixed exposure defined by a reactant pressure for a certain exposure time, the ZnO coverage in AAO membranes will transition from complete

uniformity to partial uniformity as a function of aspect ratio. This behavior has been observed for Zn coverage profiles in AAO membranes with aspect ratios from 250 to 2500 after ZnO ALD at 10 RPM and 50 °C as displayed in Fig. 4.[21]

The results in Fig. 4 were obtained using 10 RPM with no additional spacers between the DEZ precursor module and the two adjacent pumping modules. For these reaction conditions, the DEZ exposure time is 150 ms. This exposure time is sufficient for uniform Zn coverages at an aspect ratio of 250 and is not sufficient for uniform Zn coverages at an aspect ratio of 2500. The exposure times can be increased by adding spacers between the precursor module and the two adjacent pumping modules. Figure 5 shows the Zn coverage in an AAO membrane with a pore diameter of 100 nm at a faster rotation speed of 100 RPM for 0, 2, and 4 total spacers between the DEZ precursor module and the two adjacent pumping modules. The exposure times at 100 RPM for 0, 2, and 4 total spacers are 15, 30, and 45 ms, respectively. The aspect ratio of the 100 nm pores in the AAO membrane was 250.

The normalized Zn signal in Fig. 5 at the bottom of the pore at 25 μm increases from ∼0 to ∼0.125 after adding four total spacers between the DEZ precursor module and the two adjacent pumping modules. Higher normalized Zn signals would be observed at slower rotation speeds, higher reactant pressures, or for a larger number of spacers. The results in Fig. 5 are consistent with Monte Carlo simulations of ZnO ALD into the AAO membranes.[2] For example, the required DEZ exposure time for uniform coverage for an aspect ratio of 250 with a DEZ partial pressure of 0.1 Torr is 1.0 s. In contrast, the exposure time is 45 ms for the results with four total spacers in Fig. 5 at 100 RPM. A uniform Zn coverage in the AAO pores is not expected for the results in Fig. 5.

C. Al$_2$O$_3$ ALD on porous LCO electrodes

Given the ZnO ALD results on model porous AAO membranes at the slower rotation speed of 10 RPM, spatial ALD

FIG. 5. (Color online) Normalized zinc signal vs distance from top of the porous AAO membrane with a pore diameter of 100 nm. ZnO ALD films were grown using DEZ and ozone at 40 °C. ZnO spatial ALD was performed at 100 RPM using 0, 2, and 4 total spacers.

is a promising process to coat porous LCO battery electrodes. Figure 4 shows that pores in AAO membranes with aspect ratios of 250 can be coated uniformly with a rotation speed of 10 RPM. In comparison, the LCO battery electrodes have an aspect ratio of 12–25. Spatial ALD should be able to coat the porous LCO electrodes, provided that the reactant exposures are sufficient.

Cross-sectional EDS was employed to evaluate the Al$_2$O$_3$ ALD in the LCO electrodes. The Al$_2$O$_3$ ALD-coated LCO electrodes were prepared for EDS measurements using a focused ion beam (FIB) to form the cross-section. Figure 6 shows the EDS signals for a cross-section of an LCO electrode with no Al$_2$O$_3$ ALD coatings. Figures 6(a)–6(d) show EDS signals for Co, C, Al, and a mixture of these three elements, respectively.
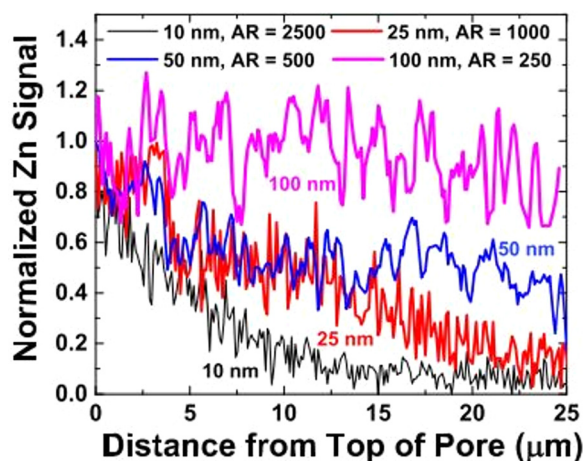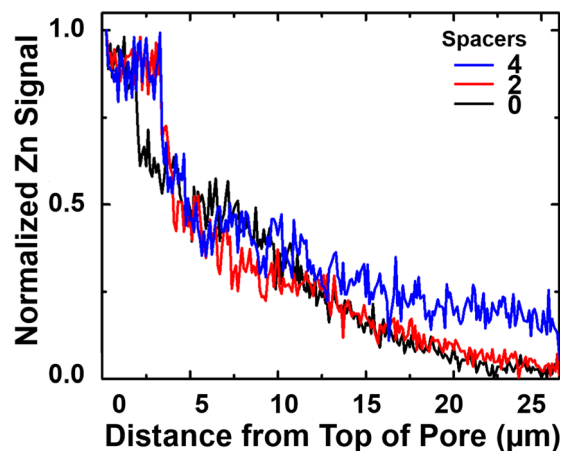
FIG. 4. (Color online) Normalized zinc signal vs distance from the top of the porous AAO membrane with pore diameters from 10 to 100 nm. ZnO ALD films were grown using DEZ and ozone at 50 °C. ZnO spatial ALD was performed at 10 RPM using no spacers. Reprinted with permission from Sharma *et al.*, J. Vac. Sci. Technol., A **34**, 01A146 (2016). Copyright 2016, American Vacuum Society.
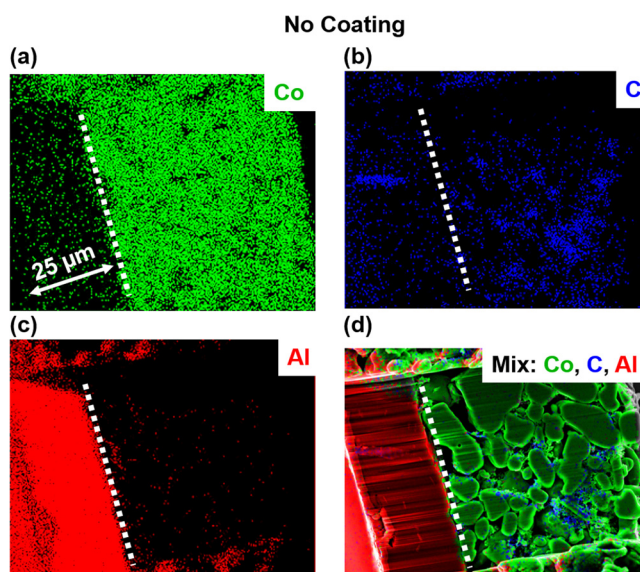
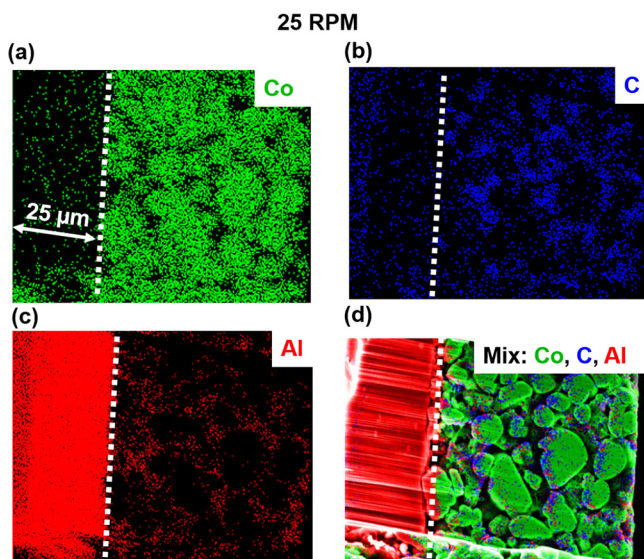FIG. 6. (Color online) Elemental maps on the LCO electrode from EDS signals for (a) Co, (b) C, (c) Al, and (d) mixture. This LCO electrode had no Al$_2$O$_3$ ALD coating. Dashed line designates the top of the Al foil.

The dashed lines in Fig. 6 show the position of the top of the Al foil. The Al foil is to the left of the dashed line. The porous electrode is to the right of the dashed line. Figure 6(a) displays the Co EDS signals from the LCO electrode material. Figure 6(b) shows the C EDS signal from the carbon additives and polymer binders. The C EDS signals are located in the areas around the Co EDS signals. Figure 6(c) displays the Al EDS signal from the Al foil. Figure 6(d) combines the Co, C, and Al EDS signals. The streaks in these images are artifacts of the FIB preparation process.

Figure 7 displays the EDS signals for a cross-section of a LCO electrode after 2000 cycles of Al_2O_3 ALD at 25 RPM. There were four total spacers between each precursor module and the two adjacent pumping modules. Figures 7(a)–7(d) show EDS signals for Co, C, Al, and a mixture of these three elements, respectively. These figures are similar to the corresponding figures in Fig. 6. However, the Al EDS signal in Fig. 7(c) shows Al in the regions around the electrode particles. These Al signals are derived from the Al_2O_3 ALD on the LCO particles and the surrounding binder. The Al signals are not observed on the FIB cut surface of the LCO particles. Al cannot be detected on the backside of the LCO particles. The LCO particles have diameters of 5–10 μm that are larger than the penetration depth of the electrons at 15 keV.

Figure 8 shows the EDS signals for a cross-section of an LCO electrode after 2000 cycles of Al_2O_3 ALD at 50 RPM. Figures 8(a)–8(d) again show EDS signals for Co, C, Al, and a mixture of these three elements, respectively. These images are similar to the corresponding ones in Fig. 7. The Al EDS signal in Fig. 8(c) again shows Al signals that are derived from the Al_2O_3 ALD on the LCO particles and the surrounding binder. However, the Al signals are slightly smaller because less Al_2O_3 ALD is deposited at the higher rotation speed of 50 RPM.

25 RPM

FIG. 7. (Color online) Elemental maps on the LCO electrode from the EDS signal for (a) Co, (b) C, (c) Al, and (d) mixture. This LCO electrode had 2000 cycles of Al_2O_3 ALD using TMA and ozone at 25 RPM and 60 °C. There were four total spacers between each precursor module and the two adjacent pumping modules. Dashed line designates the top of the Al foil.
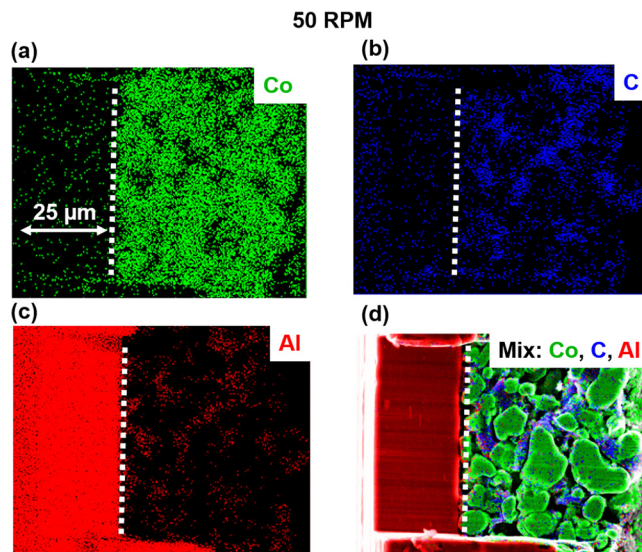
50 RPM

FIG. 8. (Color online) Elemental maps on the LCO electrode from the EDS signal for (a) Co, (b) C, (c) Al, and (d) mixture. This LCO electrode had 4 cycles of Al_2O_3 ALD using TMA and ozone at 50 RPM and 60 °C. There were four total spacers between each precursor module and the two adjacent pumping modules. Dashed line designates the top of the Al foil.

The Al signals in both Figs. 7(c) and 8(c) are uniform throughout the region around the LCO particles from the top of the electrode to the Al foil underneath the electrode. This uniformity is predicted by the Monte Carlo simulations for ALD into pores.[2] The required exposure time for an aspect ratio of 25 and a reactant partial pressure of 0.1 Torr is 10 ms. In comparison, the reactant exposure times at 25 and 50 RPM are 180 and 90 ms, respectively.

The uniformity of the Al_2O_3 ALD coatings on the LCO electrodes can be evaluated by partitioning the cross-sectional EDS maps shown in Figs. 6–8 into regions that are displayed in Figs. 9(a), 10(a), and 11(a). Average EDS signals can then be determined in each region. Regions 0 and 1 represent the Al foil. Regions 2–7 define the LCO electrode. For the uncoated LCO electrode, Fig. 9(b) reveals that the main EDS signals in the LCO electrode are Co, O, and C as expected for the LCO particles and the binder. The average Al EDS signal in regions 3–7 is 1.0 ± 0.4 wt. %. This Al EDS signal is attributed to noise from scattering from the nearby Al foil.

Figures 10(b) and 11(b) show the EDS signals for the LCO electrode coated with 2000 Al_2O_3 ALD cycles using rotation speeds of 25 and 50 RPM, respectively. The Al EDS signal is uniform across regions 3–7 in Fig. 10(b) for a rotation speed of 25 RPM. The average Al EDS signal for regions 3–7 is 6.0 ± 1.6 wt. %. This Al EDS signal is ~6 times greater than the noise measured for the control sample with no Al_2O_3 ALD coatings. The standard deviation of 1.6 wt. % Al is near the noise of 1.4 wt. % Al measured in Fig. 9(b).

The Al EDS signal is also uniform across regions 3–7 in Fig. 11(b) for a rotation speed of 50 RPM. The average Al EDS signal for regions 3–7 is 4.7 ± 1.0 wt. %. The average Al EDS signal for 50 RPM is less than the average Al EDS signal for 25 RPM. This lower Al EDS signal is consistent
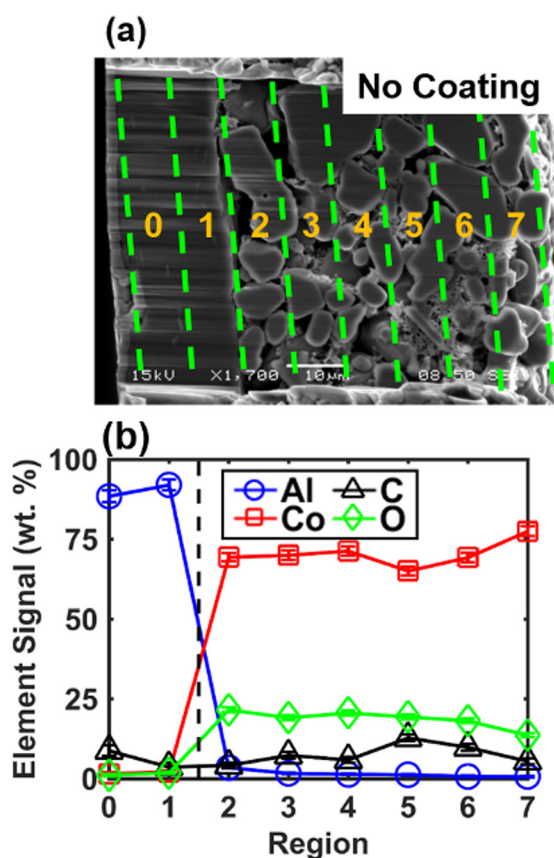
FIG. 9. (Color online) (a) Cross-sectional SEM image of the electrode with no Al_2O_3 ALD coating. (b) Average elemental signals calculated from EDS maps in Fig. 6.

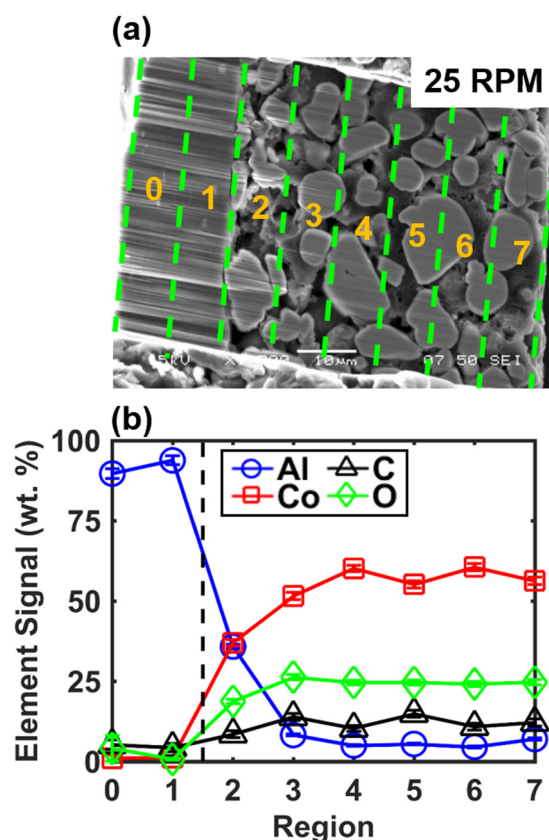FIG. 10. (Color online) (a) Cross-sectional SEM image of the electrode with 2000 cycles of Al_2O_3 ALD using TMA and ozone at 25 RPM and 60 °C. (b) Average elemental signals calculated from EDS maps in Fig. 7.

with the lower reactant exposure time at 50 RPM. The standard deviation of 1.0 wt. % Al is also near the noise level of 1.4 wt. % Al.

D. Coin cells with Al_2O_3 ALD coatings on LCO electrodes

Figure 12 shows the discharge capacity versus the discharge–charge cycle number for coin cells with and without Al_2O_3 ALD coatings on the LCO electrodes. The results are the averages over at least three separate coin cells. These Al_2O_3 ALD coatings were deposited using temporal ALD using three different reactor designs. These reactors and the reaction conditions are given in Table I. The coin cells were cycled at 0.1 C rate for the first five cycles and 1 C rate for the subsequent cycles at room temperature and 3.3–4.5 V. The error bars and data points are plotted for every ten and five discharge–charge cycles, respectively.

The discharge capacity of the coin cells with no ALD coatings fades quickly after ∼25 discharge–charge cycles. In contrast, coin cells with Al_2O_3 ALD coatings from four Al_2O_3 ALD cycles deposited using temporal ALD yield much better performances. The discharge capacities of Li-ion batteries with Al_2O_3 ALD-coated LCO electrodes after 151 discharge–charge cycles were comparable with discharge capacities of ∼98 ± 26, 122 ± 8, and 90 ± 15 mA h/g for temporal ALD reactors I, II, and III, respectively. These

full cell results are similar to earlier results that have observed the enhanced capacity stability of Li-ion battery electrodes coated by ALD.[3,37]

For comparison, the Al_2O_3 ALD coatings were also deposited using spatial ALD. Figure 13 displays the discharge capacity versus the discharge–charge cycle numbers for coin cells with and without Al_2O_3 spatial ALD coatings on the LCO electrodes. The results for the discharge capacity are the averages over at least three separate coin cells. The Al_2O_3 ALD coatings were deposited using four ALD cycles with four total spacers between each precursor module and the two adjacent pumping modules. The coin cells were again cycled at 0.1 C rate for the first five cycles and 1 C rate for the subsequent cycles at room temperature and 3.3–4.5 V.

The performances of coin cells with Al_2O_3 ALD coatings on the LCO electrodes showed comparable retention of discharge capacity after 151 discharge–charge cycles. Discharge capacities of 76 ± 10, 81 ± 36, and 56 ± 70 mA h/g were measured for rotation speeds of 10, 25, and 50 RPM, respectively. These discharge capacities are much better than the results for the uncoated LCO electrodes where the discharge capacity starts to fade after 25 discharge–charge cycles.

The increase in the error in the discharge capacities after 100 discharge–charge cycles results from one coin cell fading in the set of three coin cells prepared using rotation speeds of 25 and 50 RPM. This larger error may be a result
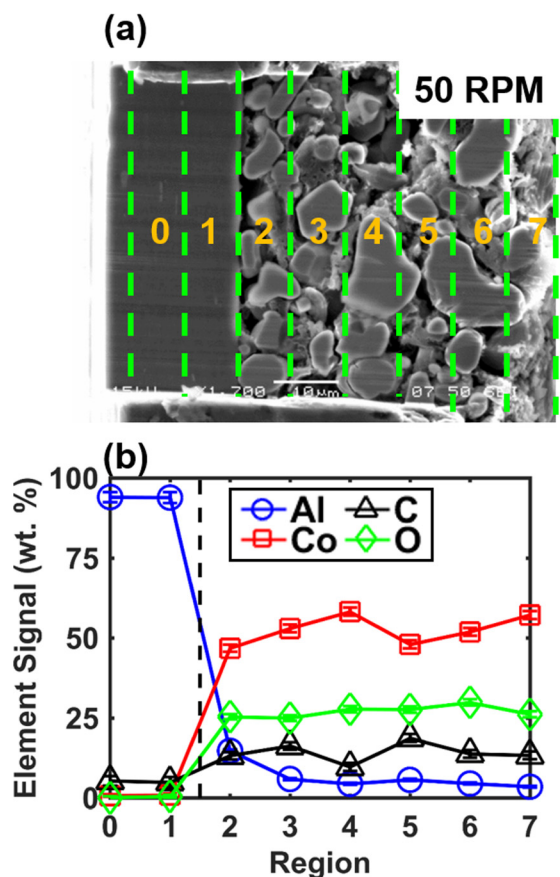
FIG. 11. (Color online) (a) Cross-sectional SEM image of the electrode with 2000 cycles of Al_2O_3 ALD using TMA and ozone at 50 RPM and 60 °C. (b) Average elemental signals calculated from EDS maps in Fig. 8.

of coin cell fabrication or problems with the uniformity of the Al_2O_3 ALD coating on the LCO electrodes at the higher rotation speeds. Reactant infiltration and uniformity of the Al_2O_3 ALD coating over the entire thickness of the porous LCO electrodes should be higher for slower rotation speeds and longer exposure zones defined by more spacers. Further
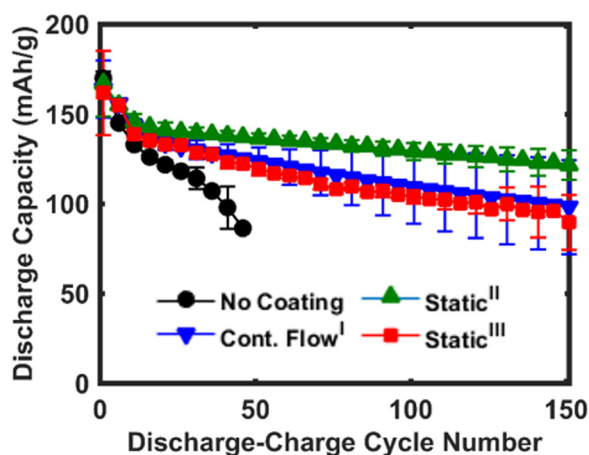
FIG. 12. (Color online) Discharge capacity vs discharge–charge cycle number for uncoated LCO electrodes and LCO electrodes coated with four cycles of Al_2O_3 ALD using temporal ALD. The temporal ALD reactors were (I) Beneq TFS 200 continuous flow reactor, (II) home-built static reactor, and (III) home-built static reactor as described in Table I.
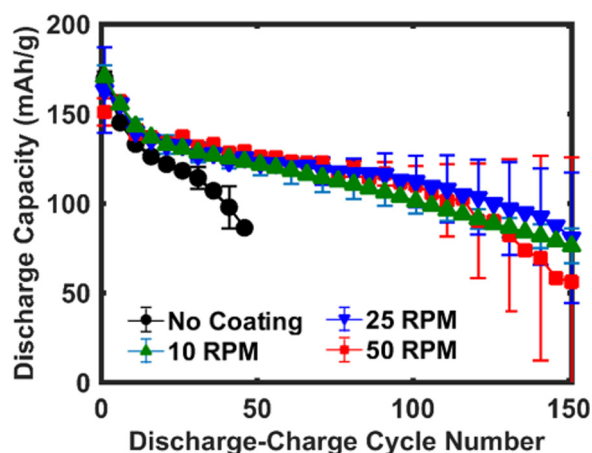
FIG. 13. (Color online) Discharge capacity vs discharge–charge cycle numbers for uncoated LCO electrodes and LCO electrodes coated with 4 cycles of Al_2O_3 ALD using spatial ALD. The spatial ALD was performed using 10, 25, and 50 RPM at 60 °C. There were four total spacers between each precursor module and the two adjacent pumping modules.

studies are needed to improve the reproducibility of the Al_2O_3 ALD coating on the LCO electrodes.

E. Roll-to-roll spatial ALD with the modular rotating cylinder reactor

Spatial ALD using the rotating cylinder reactor can be scaled up to true R2R operation. The apparatus that is currently under construction is shown in Fig. 14. This R2R spatial ALD system consists of three main components: a web handling box, a transfer box, and the rotating cylinder reactor. The web handling box is composed of two motor-controlled rollers, two tension rollers and two idler rollers. The purpose of the web handling box is to control web tension and rewind/wind operations. The transfer box consists of substrate heating and cooling regions. The web is heated using lamps with a maximum output of 1000 W. The web is cooled using a cold water heat exchanger. A baffle is used to isolate the two temperature regions.
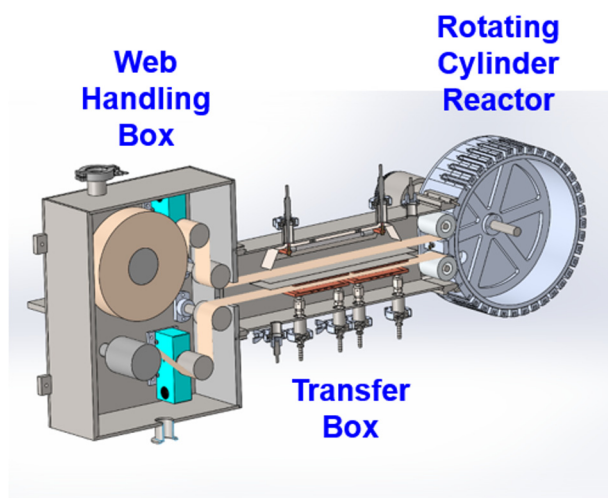

FIG. 14. (Color online) Schematic of the rotating cylinder reactor connected to the transfer box and the web handling box for scale-up to R2R operation.

The web enters the rotating cylinder reactor and comes into contact with the inner rotating cylinder. After exposure to the various reactant, pumping, purging, and spacer zones as the web travels around the circumference of the rotating inner cylinder, the web exits the rotating cylinder reactor and passes back through the transfer box. The web speed is set by the rotation of the inner rotating cylinder. The drive axle of the rotating inner cylinder is magnetically coupled to an external motor. This R2R spatial ALD system can handle a web width of ∼100 mm.

IV. CONCLUSIONS

Spatial ALD can be employed to enhance the performance of Li-ion batteries. However, porous Li-ion battery electrodes require high reactant exposures for uniform ALD coatings in their high aspect ratio electrode structures. In this work, a modular rotating cylinder reactor was utilized to coat flexible porous Li-ion battery electrodes. The modules on this reactor could be easily changed to test different reactor configurations. A variety of tests were conducted to obtain the necessary reactant exposures for spatial ALD on porous substrates. Initial experiments characterized spatial Al_2O_3 and ZnO ALD on flat, flexible metalized PET foils. These investigations revealed that slower rotation speeds and spacers between the precursor module and the two adjacent pumping modules could significantly increase the reactant exposures.

The modular rotating cylinder reactor was also used to coat flexible, porous model AAO membranes. The uniformity of the ZnO ALD coatings was dependent on the aspect ratio of the pores of the AAO membranes and the reactant exposures. Larger reactant exposures produced better uniformity in the higher aspect ratio pores. The reactant exposures were increased by adding spacers between the reactant module and the two adjacent pumping modules. In addition, the modular rotating cylinder reactor was employed for Al_2O_3 ALD on porous LCO battery electrodes. There was good uniformity of the Al_2O_3 ALD coatings on the LCO electrodes with aspect ratios of ∼12–25 for rotation speeds of 25 and 50 RPM using four total spacers between each precursor module and the two adjacent pumping modules.

Coin cells were also constructed using the ALD-coated LCO electrodes. These coin cells were tested to determine battery performances. The discharge capacity of the Al_2O_3 ALD-coated LCO battery electrodes was measured versus the number of charge-discharge cycles. Both temporal and spatial ALD processing yielded higher capacity stability than the uncoated LCO electrodes. Temporal and spatial ALD had similar results for improved battery performance. Plans are also described for scale-up to R2R spatial ALD using the modular rotating cylinder reactor.

ACKNOWLEDGMENTS

[1]S. M. George, Chem. Rev. **110**, 111 (2010).

[2]J. W. Elam, D. Routkevitch, P. P. Mardilovich, and S. M. George, Chem. Mater. **15**, 3507 (2003).

[3]Y. S. Jung, A. S. Cavanagh, A. C. Dillon, M. D. Groner, S. M. George, and S. H. Lee, J. Electrochem. Soc. **157**, A75 (2010).

[4]Y. S. Jung, A. S. Cavanagh, L. A. Riley, S. H. Kang, A. C. Dillon, M. D. Groner, S. M. George, and S. H. Lee, Adv. Mater. **22**, 2172 (2010).

[5]M. Bettge, Y. Li, B. Sankaran, N. D. Rago, T. Spila, R. T. Haasch, I. Petrov, and D. P. Abraham, J. Power Sources **233**, 346 (2013).

[6]H. M. Cheng, F. M. Wang, J. P. Chu, R. Santhanam, J. Rick, and S. C. Lo, J. Phys. Chem. C **116**, 7629 (2012).

[7]L. A. Riley, A. S. Cavanagh, S. M. George, Y. S. Jung, Y. F. Yan, S. H. Lee, and A. C. Dillon, ChemPhysChem **11**, 2124 (2010).

[8]I. D. Scott, Y. S. Jung, A. S. Cavanagh, Y. F. An, A. C. Dillon, S. M. George, and S. H. Lee, Nano Lett. **11**, 414 (2011).

[9]Y. He, X. Q. Yu, Y. H. Wang, H. Li, and X. J. Huang, Adv. Mater. **23**, 4938 (2011).

[10]H. Kim, J. T. Lee, D. C. Lee, A. Magasinski, W. I. Cho, and G. Yushin, Adv. Energy Mater. **3**, 1308 (2013).

[11]E. M. Lotfabad, P. Kalisvaart, K. Cui, A. Kohandehghan, M. Kupsta, B. Olsen, and D. Mitlin, Phys. Chem. Chem. Phys. **15**, 13646 (2013).

[12]M. P. Yu, W. J. Yuan, C. Li, J. D. Hong, and G. Q. Shi, J. Mater. Chem. A **2**, 7360 (2014).

[13]J. S. Jung, A. S. Cavanagh, L. Gedvilas, N. E. Widjonarko, I. D. Scott, S. H. Lee, G. H. Kim, S. M. George, and A. C. Dillon, Adv. Energy Mater. **2**, 1022 (2012).

[14]P. Poodt, D. C. Cameron, E. Dickey, S. M. George, V. Kuznetsov, G. N. Parsons, F. Roozeboom, G. Sundaram, and A. Vermeer, J. Vac. Sci. Technol., A **30**, 010802 (2012).

[15]P. R. Fitzpatrick, Z. M. Gibbs, and S. M. George, J. Vac. Sci. Technol., A **30**, 01A136 (2012).

[16]D. Levy, D. Freeman, S. F. Nelson, P. J. Cowdery-Corvan, and L. M. Irving, Appl. Phys. Lett. **92**, 192101 (2008).

[17]D. Levy, S. F. Nelson, and D. Freeman, J. Disp. Technol. **5**, 484 (2009).

[18]P. Poodt, A. Lankhorst, F. Roozeboom, K. Spee, D. Maas, and A. Vermeer, Adv. Mater. **22**, 3564 (2010).

[19]P. S. Maydannik, T. O. Kaariainen, and D. C. Cameron, Chem. Eng. J. **171**, 345 (2011).

[20]P. S. Maydannik, T. O. Kaariainen, and D. C. Cameron, J. Vac. Sci. Technol., A **30**, 01A122 (2012).

[21]K. Sharma, D. Routkevitch, N. Varaksa, and S. M. George, J. Vac. Sci. Technol., A **34**, 01A146 (2016).

[22]K. Sharma, R. A. Hall, and S. M. George, J. Vac. Sci. Technol., A **33**, 01A132 (2015).

[23]E. Dickey and W. A. Barrow, J. Vac. Sci. Technol., A **30**, 021502 (2012).

24A. S. Yersak, Y. C. Lee, J. A. Spencer, and M. D. Groner, J. Vac. Sci. Technol., A 32, 01A130 (2014).

25P. S. Maydannik *et al.*, J. Vac. Sci. Technol., A 32, 051603 (2014).

26P. Poodt, A. Mameli, J. Schulpen, W. M. M. Kessels, and F. Roozeboom, J. Vac. Sci. Technol., A 35, 021502 (2017).

27K. P. Musselman, D. Munoz-Rojas, R. L. Z. Hoye, H. Sun, S. L. Sahonta, E. Croft, M. L. Bohm, C. Ducati, and J. L. MacManus-Driscoll, Nanoscale Horiz. 2, 110 (2017).

28P. S. Maydannik, A. Plyushch, M. Sillanpaa, and D. C. Cameron, J. Vac. Sci. Technol., A 33, 031603 (2015).

29P. Poodt, J. V. Lieshout, A. Illiberi, R. Knaapen, F. Roozeboom, and A. V. Asten, J. Vac. Sci. Technol., A 31, 01A108 (2013).

30J. W. Elam, J. A. Libera, M. J. Pellin, and P. C. Stair, Appl. Phys. Lett. 91, 243105 (2007).

31D. Goldstein, J. A. McCormick, and S. M. George, J. Phys. Chem. C 112, 19530 (2008).

32A. A. Dameron, D. Seghete, B. B. Burton, S. D. Davidson, A. S. Cavanagh, J. A. Bertrand, and S. M. George, Chem. Mater. 20, 3315 (2008).

33S. Suh, S. Park, H. Lim, Y. J. Choi, and C. S. Hwang, J. Vac. Sci. Technol., A 30, 051504 (2012).

34P. Poodt, V. Tiba, F. Werner, J. Schmidt, A. Vermeer, and F. Roozeboom, J. Electrochem. Soc. 158, H937 (2011).

35M. D. Groner, F. H. Fabreguette, J. W. Elam, and S. M. George, Chem. Mater. 16, 639 (2004).

36S. E. Potts, W. Keuning, E. Langereis, G. Dingemans, M. C. M. van de Sanden, and W. M. M. Kessels, J. Electrochem. Soc. 157, P66 (2010).

37Y. S. Jung, P. Lu, A. S. Cavanagh, C. Ban, G. H. Kim, S. H. Lee, S. M. George, S. J. Harris, and A. C. Dillion, Adv. Energy Mater. 3, 213 (2013).